Short communication

Enhanced triple-phase boundary density in infiltrated electrodes for solid oxide fuel cells demonstrated by high-resolution tomography

CrossMark

Masashi Kishimoto[*], Marina Lomberg, Enrique Ruiz-Trejo, Nigel P. Brandon

Department of Earth Science and Engineering, Imperial College London, London SW7 2AZ, United Kingdom

HIGHLIGHTS

- Microstructure of nickel-infiltrated GDC scaffold is analyzed by FIB-SEM.
- TPB density and mean particle/pore sizes are quantified.
- Infiltrated electrodes have eight times larger TPB density than conventional electrodes.
- Shorter TPB segments are generated by infiltration than conventional methods.
- Infiltration technique has a potential to better control porous microstructure.
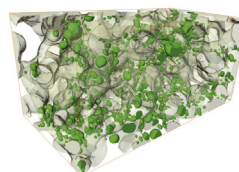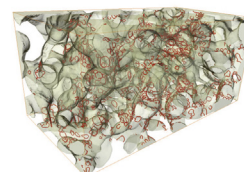
GRAPHICAL ABSTRACT
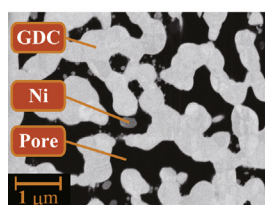
GDC porous scaffold with 1 time nickel infiltration

ARTICLE INFO

ABSTRACT

This paper, for the first time, demonstrates the three-dimensional imaging of nano-particle infiltrated Ni−GDC (gadolinia-doped ceria) electrodes using focused ion beam tomography. Microstructural parameters of the actual electrode microstructure are quantified, such as volume fraction, TPB density and mean particle/pore sizes. These microstructural parameters reveal that the infiltrated electrodes have eight times larger TPB density than conventional electrodes fabricated by powder mixing and sintering methods. Comparison between the infiltrated electrodes and conventional electrodes indicates that the infiltrated electrodes have a greater potential to independently control metal particle size, porosity and TPB density, which is a significant advantage in developing design optimized electrode microstructures.

© 2014 Elsevier B.V. All rights reserved.

1. Introduction

Solid oxide fuel cells (SOFCs) are promising energy conversion devices because they can convert the chemical energy of fuels into electrical energy in an efficient and clean manner. It is generally accepted that electrode microstructure plays an important role in determining the performance and durability of SOFCs. They are required to contain as many active reaction sites, termed triple-phase boundaries (TPBs), as possible to promote the electrochemical reaction. At the same time, effective transport pathways need to be established to and from each TPB. Therefore, the microstructure-performance relationships need to be understood in order to develop optimum electrodes.

Infiltration techniques are receiving increasing attention as alternative fabrication methods to prepare SOFC electrodes because they enable relatively easier control of composition and particle sizes compared with conventional powder mixing and sintering methods. The porous structure is first fabricated on top of the dense electrolyte with a single solid phase (scaffold structure), to which

the other solid phase is introduced in the form of nanoparticles (~10 nm). From this technique we can expect a significant increase in the TPB density in the electrodes. A summary of the history and the latest developments in infiltration techniques for this application can be found in reviews by Jiang [1], and Vohs and Gorte [2].

Three-dimensional (3D) imaging technique, such as focused ion beam scanning electron microscopy (FIB-SEM) and X-ray nano CT, are finding increasing application in the study of complex electrode microstructures [3–6]. Through the development and application of quantification methodologies and numerical simulation models, new insights have been generated, which offer the prospect of optimizing electrode microstructure to further improve performance and durability [7–11]. However, microstructural information related to infiltrated electrodes still remains limited, mainly due to the difficulty in imaging the bimodal structures, scaffolds and nano-particles, where the infiltrated catalyst particles are generally significantly smaller than those used to construct the scaffold.

In this study, the 3D microstructure of infiltrated Ni–GDC (gadolinia-doped ceria) electrodes was obtained using FIB-SEM, and microstructural parameters that characterize the porous structures were quantitatively evaluated, such as TPB density and particle/pore sizes. By comparison of these quantified parameters between infiltrated and conventional electrodes, several advantages of employing infiltration techniques are clearly elucidated, and strategies to further improve the electrode microstructure are proposed.

2. 3D imaging and reconstruction

The GDC scaffold was fabricated on an 8YSZ electrolyte disk (Fuel Cells Materials) using a custom ink and sintered at 1350 °C for 2 h. Nickel nanoparticles were then infiltrated into the scaffold by introducing $Ni(NO_3)_2$ solution from the top of the scaffold followed by decomposition at 500 °C for 0.5 h. More details can be found elsewhere [12,13].

The anode samples were reduced under a hydrogen atmosphere and impregnated with epoxy resin (Specifix20, Struers) under vacuum conditions so that the pores of the anodes were easily distinguished in the SEM imaging. The cured samples were cut and mechanically polished to have a flat cross-section. The 3D microstructure of the anodes was imaged by an Auriga (Zeiss) FIB-SEM system. The backscattered electron (BSE) detector was used for imaging the Ni–GDC electrodes in order to distinguish the two solid phases in the SEM images. Regions were selected for the microstructural analysis and segmented based on image brightness. After alignment and segmentation, the 3D porous microstructure was reconstructed in a virtual field. From the reconstructed structures, phase volume fractions, surface information, particle/pore size and TPB density were quantified. Details of the quantification methodologies are found elsewhere [14,15]. Commercial image processing software, Avizo (Mercury Computer Systems, Inc.), was used for the alignment, segmentation, 3D reconstruction and some of the quantification of the microstructural parameters.

Here, three different microstructures were fabricated and imaged. The first was the virgin scaffold structure. As no nanoparticles were infiltrated in the structure, a relatively lower magnification can be used to get larger field of view. The second was an electrode with one-time infiltration. Higher magnification was required to capture the nanoparticles, which inevitably reduces the field of view. The third was an electrode with ten-time infiltration. It was possible to widen the field of view for the third sample, compared to that used with the second, as the nickel particles were larger. In this paper, these samples are labeled as GDC

scaffold, Ni(1)–GDC and Ni(10)–GDC, respectively. Electrochemical performance of the infiltrated electrodes prepared in our laboratory has been reported previously [12], where ten-time infiltration electrodes were found to be functioning as technologically useful SOFC electrodes (the total area specific resistance of the electrode was measured 0.16 Ω cm^2 at 690 °C, with 0.05 Ω cm^2 associated with the charge-transfer process). Although the electrodes tested in the previous study used polymeric beads in the GDC ink to increase
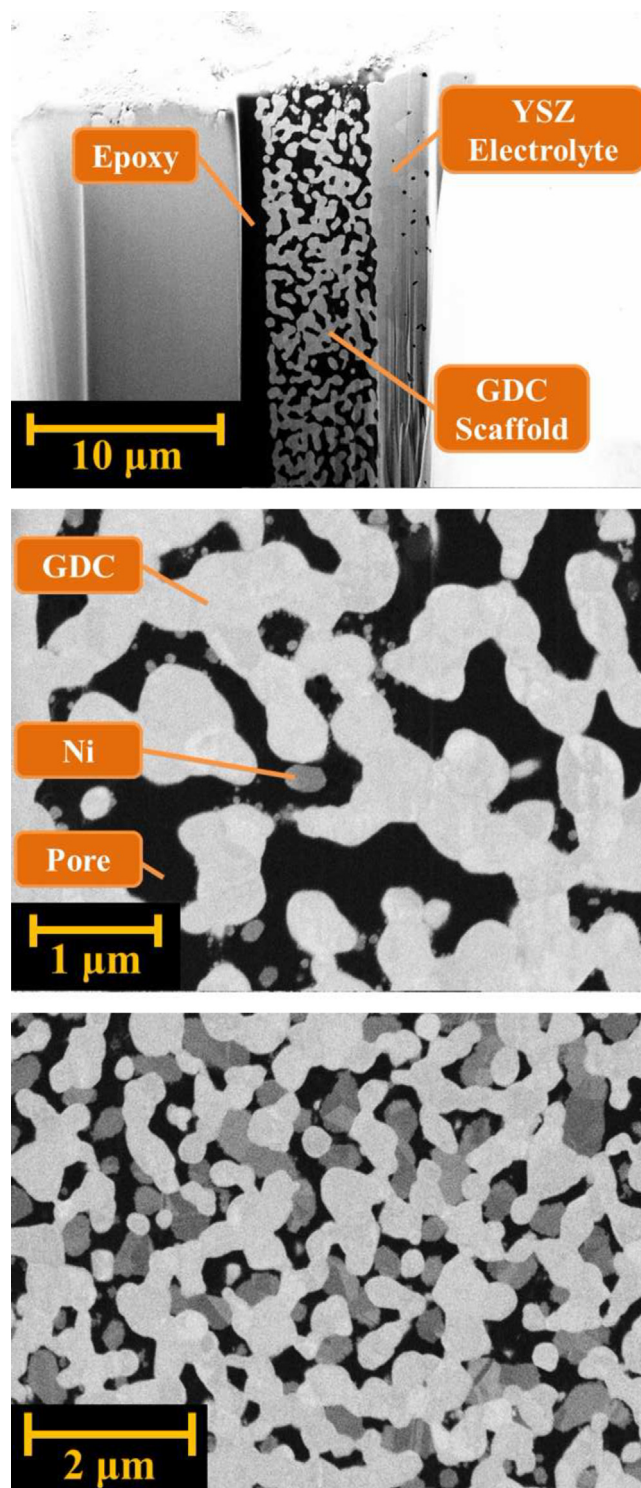

Fig. 1. Cross-sectional 2D images of the anode samples. (a) GDC scaffold (b) Ni(1)–GDC (c) Ni(10)–GDC.

porosity, other fabrication conditions such as initial particle sizes, sintering temperature and the amount of nickel loading were the same.

3. Results and discussion

Fig. 1 shows the 2D slice images of the Ni–GDC anode structures. Slice and view movies are also shown in the supplementary results. It was found that the back-scattered electron detector used in the SEM imaging was highly effective in distinguishing the three different phases in the Ni–GDC electrodes, being an improvement over the in-lens secondary electron detector commonly used to image Ni–YSZ electrodes. Also, inhomogeneous brightness (shadowing effect), which sometimes appears on the images when using secondary electron detectors, does not appear on the images obtained in this study. This is because the backscattered electrons usually have higher energy than secondary electrons. The homogeneous brightness and contrast make the image segmentation

significantly easier and more reliable. Particles with the size of ~10 nm were successfully imaged using a lower electron acceleration voltage (1.5 kV). The distribution of the infiltrated nickel particles was found to be homogeneous in the thickness direction of the anode (corresponding to the horizontal direction in the figures). Fig. 2 shows the reconstructed 3D structure of the Ni(1)–GDC and Ni(10)–GDC samples, which also confirms that the nickel particles are homogeneously distributed inside the scaffold.

Table 1 summarizes the sample size, voxel size and the quantified microstructural parameters of the samples. Typical values found in a conventional electrode (Ni–YSZ, Ni:YSZ = 50:50 vol.% [14]) are also shown for comparison. First of all the GDC scaffolds in the three structures imaged in this study have equivalent features because they have similar volume fraction, surface-to-volume ratio and average particle sizes. This ensures that the structures obtained from Ni(1)–GDC and Ni(10)–GDC are still large enough to be representative of the entire anode structure. The GDC particle sizes are close to that found in the conventional
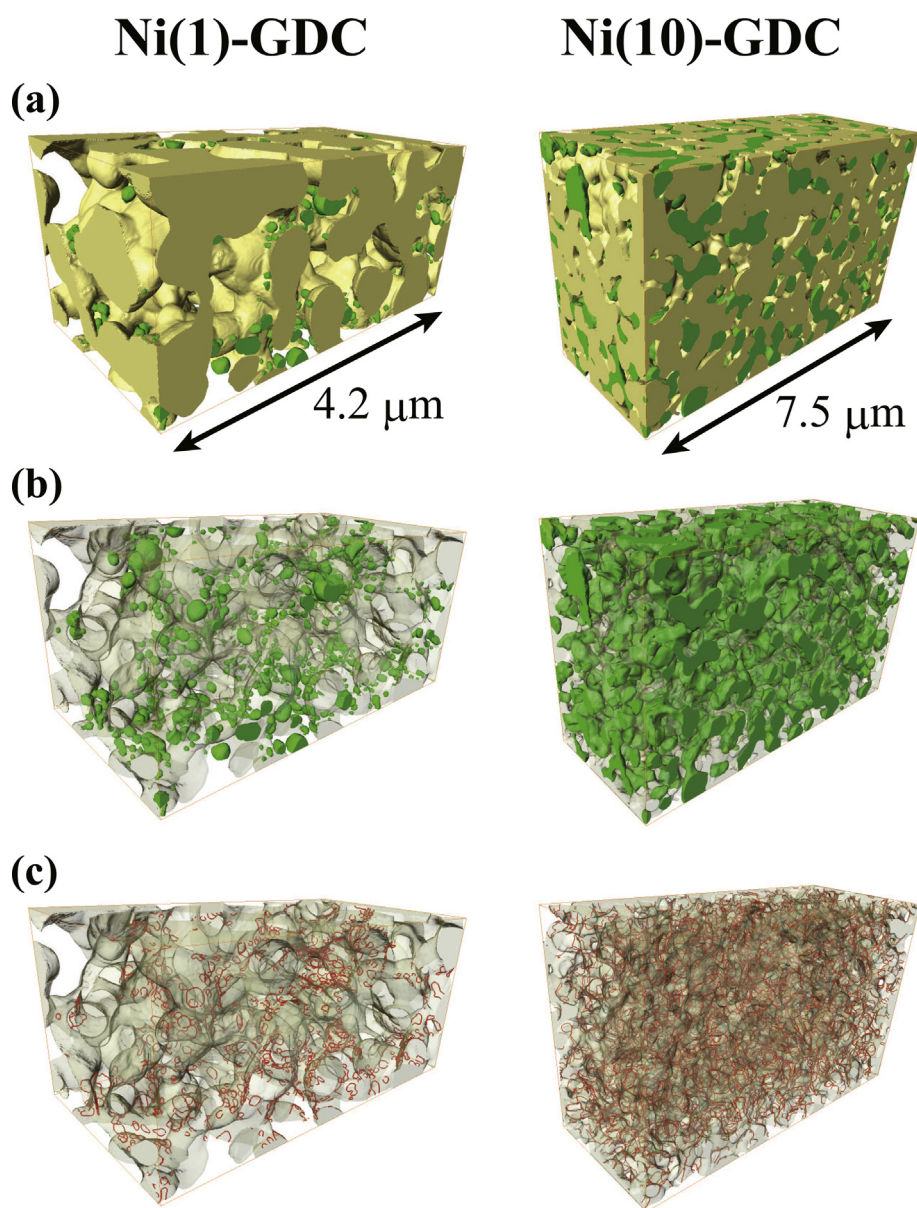

Fig. 2. Reconstructed 3D microstructure of Ni(1)–GDC and Ni(10)–GDC samples. (a) Ni–GDC (green: Ni, yellow: GDC), (b) Ni with GDC (transparent gray) and (c) TPB lines with GDC (transparent gray). (For interpretation of the references to colour in this figure legend, the reader is referred to the web version of this article.)

Table 1
Microstructural parameters.

		GDC scaffold	Ni(1)–GDC	Ni(10)–GDC	Conventional Ni–YSZ [14]
Sample size [μm]	X	18.0	4.28	7.50	19.2
	Y	4.50	2.00	4.50	8.51
	Z	5.25	2.25	3.00	6.20
Voxel size [nm]	X	30.0	5.0	10.0	26.6
	Y	30.0	5.0	10.0	26.6
	Z	30.0	10.0	10.0	62.0
Volume fraction [%]	Ni	0.00	1.29	19.8	25.3
	GDC/YSZ	57.1	56.9	60.2	25.1
	Pore	42.9	41.8	20.1	49.6
Particle/pore size [μm]	Ni	n/a	0.102	0.354	1.38
	GDC/YSZ	0.844	0.748	0.706	0.730
	Pore	0.667	0.594	0.300	1.74
Surface-to-volume ratio [$\mu m^2\ \mu m^{-3}$]	Ni	n/a	60.0	16.2	3.56
	GDC/YSZ	6.44	6.82	7.94	7.51
	Pore	8.58	10.0	21.1	4.12
TPB density [$\mu m\ \mu m^{-3}$]		n/a	11.0	18.4	2.49

electrode, although the volume fraction is more than double. On the other hand, the nickel volume fraction and particle sizes are significantly smaller than those found in the conventional electrode. The smaller metal particle sizes are a result of the fact that the decomposition temperature for the nickel particles (500 °C) is significantly lower than the typical sintering temperature for the conventional electrodes (~1400 °C). There is no percolating cluster of the nickel phase in both infiltrated samples. However, as the GDC is a mixed ionic and electronic conductor (MIEC), and both conductivities are comparable at the typical operating temperature of SOFCs [16], the negative effect of the lower nickel connectivity on the electrode performance may be less significant than in the conventional Ni–YSZ electrodes, where the YSZ is a pure ionic conductor.

In general, smaller nickel particle sizes are preferable for larger TPB density. From the quantified parameters, the TPB densities in the infiltrated electrodes were found to be one-order of magnitude larger than those in the conventional electrode. This has been suggested by several researchers [1,2,16]; however, this is the first time that this has been quantitatively confirmed from a tomography dataset. Fig. 3 shows the cumulative length distributions of the TPB segments in the infiltrated samples, and also that of the conventional Ni–YSZ electrode. 80% accumulation appears at 350 nm, 1.3 μm and 1.7 μm in Ni(1)–GDC, Ni(10)–GDC and Ni–YSZ samples, respectively. This indicates that the single time infiltration creates

much smaller TPB segments than the conventional powder mixing and sintering process. Although multiple infiltrations inevitably increase the length of the TPB segments, they are still shorter than those found in conventional electrodes. Shorter TPB segments are consistent with the smaller particle sizes found in the above analysis, and one of the reasons why the infiltrated electrodes have larger TPB density.

In conventional electrodes it is also possible to increase the TPB density by reducing the initial particle size. However, the high temperature required to sinter the ceramic particles (1300–1400 °C) makes it difficult to retain the smaller particle sizes for the nickel oxide particles. Moreover, smaller particle sizes inevitably result in smaller pore size, increasing the gas diffusion resistance. Therefore, reducing particle sizes may not be the ideal approach for conventional electrodes to improve the overall electrochemical performance.

On the other hand, in the infiltrated electrodes, it is easier to retain a smaller nickel particle size as the nickel phase does not experience a high sintering temperature during fabrication. Also, it is possible to independently control the porosity and pore sizes by optimizing the scaffold structure. In the electrodes analyzed in this study, gas diffusion through the electrode might be inhibited because the average pore size (0.3 μm) is smaller than those in conventional electrodes and falls in the region where the Knudsen effect appears [17]. However, it is possible to add pore former, such as carbon black, to increase the porosity of the GDC scaffold up to ca. 60% so that the anodes after infiltration have similar porosity and pore sizes as the conventional electrodes. Although the volume of the GDC phase is expected to decrease ca. 33% by adding pore former, and subsequently the TPB density would be expected to decrease by a similar percentage, it would remain significantly larger than those in conventional electrodes. This will be explored in further work.

Since GDC is a mixed conductor, the entire surface of the GDC phase is potentially active for the electrochemical reaction. Therefore the contact surface area between the GDC and pore phases (double-phase boundary: DPB) is also of interest. The value was found to be 2.89 and 1.33 $\mu m^2\ \mu m^{-3}$ in Ni(10)–GDC and Ni–YSZ, respectively, where the values were normalized by the total reconstructed volume, being a factor of two greater for the infiltrated electrode. However, due to the significantly higher electronic conductivity of the infiltrated nickel particles than the GDC, the electrochemical reaction is likely to preferably occur on the DPB adjacent to the TPB (i.e. we can view this as an extended TPB area). Although the size of the extended TPB area on the DPB remains an
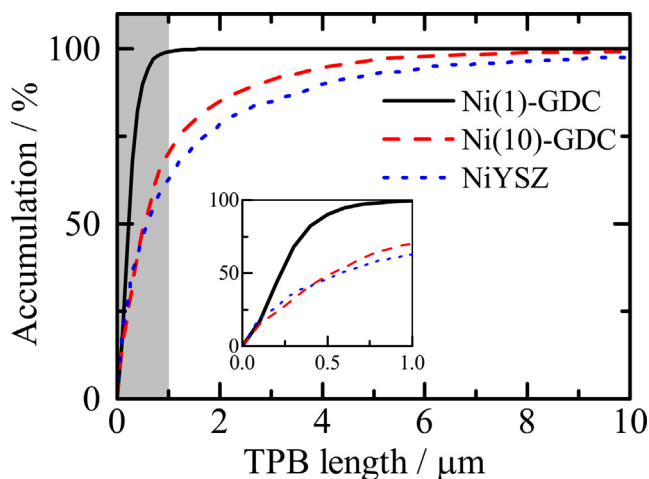

Fig. 3. Cumulative length distribution of the TPB segments.

open question, the larger TPB density revealed in this study for the infiltrated electrodes would be expected to result in a larger extended TPB area, enhancing electrode performance.

As discussed above, the infiltration technique offers a means to independently control the TPB density and pore size to improve both electrochemical activity and gas diffusivity in SOFC electrodes. This offers us the opportunity to start to design electrodes around specific performance requirements. For example, the emerging high resolution 3D printing technology enables fabrication of complex ceramic structures at the micrometer length scale. Optimal GDC and other scaffold structures could then be designed and accurately fabricated to enhance both the transport and mechanical properties, to which nano metal particles are infiltrated to form the TPB network. Although several issues have to be demonstrated with infiltrated electrodes, such as long-term stability at elevated temperatures, this paper emphasizes the potential of the approach to break the constraints evident in the fabrication of conventional electrodes, to deliver higher performance.

4. Conclusions

In this paper we have, for the first time, demonstrated the 3D imaging of nano-particle infiltrated Ni—GDC electrodes using FIB tomography. Use of low acceleration voltage (1.5 kV), high magnification and a backscattered electron detector enabled imaging of the nano nickel particles, distinguishing the two solid phases based on image contrast. Microstructural parameters quantified from actual 3D microstructures reveal that the infiltrated electrodes have eight times larger TPB density than conventional electrodes. Comparison between the infiltrated electrodes and conventional electrodes indicates that the infiltrated electrodes have a greater potential to independently control metal particle size, porosity and TPB density, which is a significant advantage in realizing design led optimization of electrode microstructures. More thorough analysis and optimization of the infiltrated electrodes using experimental measurement, microstructural analysis and numerical simulation will be reported in the future.

Appendix A. Supplementary data

Supplementary data related to this article can be found at http://dx.doi.org/10.1016/j.jpowsour.2014.05.038.

References

[1] S.P. Jiang, Int. J. Hydrogen Energy 37 (2012) 449.
[2] J.M. Vohs, R.J. Gorte, Adv. Mater. 21 (2009) 943.
[3] J.R. Wilson, W. Kobsiriphat, R. Mendoza, H.-Y. Chen, J.M. Hiller, D.J. Miller, K. Thornton, P.W. Voorhees, S.B. Adler, S.A. Barnett, Nat. Mater. 5 (2006) 541.
[4] H. Iwai, N. Shikazono, T. Matsui, H. Teshima, M. Kishimoto, R. Kishida, D. Hayashi, K. Matsuzaki, D. Kanno, M. Saito, H. Muroyama, K. Eguchi, N. Kasagi, H. Yoshida, J. Power Sources 195 (2010) 955.
[5] P.R. Shearing, Q. Cai, J.I. Golbert, V. Yufit, C.S. Adjiman, N.P. Brandon, J. Power Sources 195 (2010) 4804.
[6] N. Vivet, S. Chupin, E. Estrade, T. Piquero, P.L. Pommier, D. Rochais, E. Bruneton, J. Power Sources 196 (2011) 7541.
[7] J.R. Wilson, J.S. Cronin, S.A. Barnett, Scr. Mater. 65 (2011) 67.
[8] M. Kishimoto, K. Miyawaki, H. Iwai, M. Saito, H. Yoshida, Fuel Cells 13 (2013) 476.
[9] N. Shikazono, D. Kanno, K. Matsuzaki, H. Teshima, S. Sumino, N. Kasagi, J. Electrochem. Soc. 157 (2010) B665.
[10] R. Clague, P.R. Shearing, P.D. Lee, Z. Zhang, D.J.L. Brett, A.J. Marquis, N.P. Brandon, J. Power Sources 196 (2011) 9018.
[11] T. Carraro, J. Joos, B. Rüger, A. Weber, E. Ivers-Tiffée, Electrochim. Acta 77 (2012) 315.
[12] M. Lomberg, E. Ruiz-Trejo, G. Offer, J. Kilner, N. Brandon, ECS Trans. 57 (2013) 1349.
[13] E. Ruiz-Trejo, J.T.S. Irvine, Solid State Ionics 252 (2013) 157.
[14] M. Kishimoto, H. Iwai, M. Saito, H. Yoshida, J. Power Sources 196 (2011) 4555.
[15] M. Kishimoto, H. Iwai, K. Miyawaki, M. Saito, H. Yoshida, J. Power Sources 223 (2013) 268.
[16] W. Zhu, D. Ding, C. Xia, Electrochem. Solid-State Lett. 11 (2008) B83.
[17] M. Kishimoto, H. Iwai, M. Saito, H. Yoshida, in: Proceeding 14th Int. Heat Transf. Conf., 2010. IHTC14—22495.